

Dynamic Evolution Mechanism of A Rock Slope with Discontinuities Under Earthquake Motions Using Shaking Table Tests

Hanxu Zhou

Shanghai Jiao Tong University

Ailan Che (✉ alche@sjtu.edu.cn)

Shanghai Jiao Tong University <https://orcid.org/0000-0003-3523-2832>

Renjie Zhu

Shanghai Jiao Tong University

Research Article

Keywords: Rock slope, Shaking table, Discontinuous joints, Wave field propagation characteristics, Dynamic evolution, Safety factor.

Posted Date: August 6th, 2021

DOI: <https://doi.org/10.21203/rs.3.rs-680579/v1>

License:   This work is licensed under a Creative Commons Attribution 4.0 International License.

[Read Full License](#)

Version of Record: A version of this preprint was published at Environmental Earth Sciences on November 23rd, 2021. See the published version at <https://doi.org/10.1007/s12665-021-10102-0>.

Abstract

Under the impact of earthquake, even if the slopes do not fail, the integrity of rock slope structure would be damaged subjected to the seismic motion. The process of damage, destruction and failure for slopes is characterized by the dynamic evolution of stability. In the areas with active tectonic activities, frequent earthquakes have a significant effect on the attenuation of slope stability. To investigate the dynamic evolution of a rock slope under earthquake motions, a series of shaking table tests were performed. An artificial synthetic earthquake seismic wave was adopted to investigate the horizontal acceleration response. The results show that the wave field propagation results in M_{PGA} values for the slope body above the tuff structural surface are larger than those inside the slope, and a maximum value of 3.7 is observed at slope crest. The structural surface results in a mutation of the acceleration response, which is not conducive to the slope stability. The modeled slope entered the plastic stage (input motion of 2.97 m/s^2) earlier than landslides occurred (input motion of 4.46 m/s^2). In addition, the safety factor of the sliding blocks was calculated based on pseudo static analysis. A good correspondence was found between the safety factors and the failure mode of the slope. The damage evolution process for the rock slope can be divided into three stages: an elastic stage ($K_s=1.6-4.7$), a plastic stage ($K_s=0.8-1.6$), and a damage stage ($K_s<0.8$).

1. Introduction

Earthquakes are one of the primary causes of landslides. The complicated influence of earthquakes on landslides is an important research topic (An et al., 2015; Yang et al., 2015). Landslides that occurred during the Wenchuan earthquake provide significant data for landslide research. The 2008 Wenchuan earthquake ($M_s = 8.0$, epicenter located at 31.0°N , 103.4°E) was triggered by reactivation of Longmenshan fault zone on May 12, 2008 (Yin et al., 2009). More than 56,000 earthquake-triggered landslide disasters were discovered through aerial photographs and remote sensing images (Dai et al., 2011). Landslides can be considered the major secondary disasters associated with the Wenchuan earthquake (Huang and Li, 2009). In the decade since the Wenchuan earthquake, disturbances such as smaller earthquakes have resulted in new damage development for geological disasters (Tang, 2010). In June 2017, the Maoxian landslide occurred, caused by the potential impact of the Wenchuan earthquake 9 years later (Yin et al., 2017). The dynamic evolution process of landslides urgently needs to be understood.

Layered rock slopes with weak intercalated layers are common geologic bodies, and their response under earthquake motion is of great significance to the surrounding infrastructure (Fan et al., 2016a, b). The existing research results can provide important guidelines for the study of the dynamic response characteristics of bedding slopes and reverse bedding slopes (Yang et al., 2014). Chen et al. (2016) investigated the effect of weak intercalation on slope stability with large-scale shaking table model tests, which were conducted to study the dynamic response of rock slope models with weak intercalation. The experimental results indicated that the stability of a slope with a counter-tilt weak intercalation can be

worse than that of other slopes with horizontal weak intercalation. Fan et al. (2016b) investigated the dynamic response of slopes parallel to geological bedding (bedding slopes) and slopes that cross-cut geological bedding (counter-bedding slopes). The results indicated that the dynamic failure modes of bedding slopes and counter-bedding slopes are different. The former occurs mainly through vertical tensile cracks at the rear of the slope, bedding slide of the strata along the weak intercalation, and rock collapse from the slope crest; the latter occurs mainly through staggered horizontal and vertical fissures, extrusion of the weak intercalation, and breakage at the slope crest. Many studies have focused on the dynamic response characteristics and dynamic stability of rock slopes under earthquake loading (Chen et al., 2016; Lee et al., 2007; Liu et al., 2014; Xu et al., 2013; Xu and Yan, 2014; Yang et al., 2014; Fan et al., 2016a, b). Given these results, a better understanding of the dynamic evolution of rock slopes containing discontinuities under earthquake excitation is needed.

The understanding of rock slope dynamic evolution is the design basis for landslide prevention and control. The failure mechanism and dynamic response characteristics of a rock slope are also the foundation for dynamic stability evaluation of the slope under seismic loading (Dong et al., 2011; Yang et al., 2012). A number of previous studies have aimed to analyze the dynamic response of rock slopes under earthquake motions and have achieved some important results. The methods for analyzing slope dynamic responses under seismic excitation include analytical methods (Yang, 2007; Yang, 2009), numerical simulation methods (Shen and Karakus, 2013), and physical simulation methods (Li et al., 2009; Dong et al., 2011; Sahoo et al., 2015). Numerical methods have been an important addition to traditional slope research methods for investigation of the dynamic response of rock slopes (Wakai et al., 2008). Numerical methods have been developed and applied because of their enhanced ability to simulate actual failure mechanisms (Quecedo, 2004; Babanouri, 2017). However, these methods are difficult to apply owing to the lack of earthquake recordings resulting from the random occurrence of earthquakes. Thus, numerical methods cannot accurately evaluate seismic response. Therefore, laboratory model experiments, i.e., shaking table tests, are required for further study of the dynamic response of rock slopes. For complex slope structures, seismic modeling is one of the most useful and powerful tools for studying the effects of the propagation of seismic waves generated by ground motion. With the development of experimental technology, shaking table tests have been widely used to study the seismic response of various types of lithological combinations and structures, particularly slopes with discontinuous joints and slopes with weak intercalation (Chen et al., 2016). In shaking table tests, the response of the slope can be studied under different ground motion inputs and waveforms with varying model sizes. As a result, the dynamic response of the slope can be accurately obtained (Lin, 2006; Yang, 2012). Therefore, shaking table tests have become one of the best methods for studying rock slopes, and can reflect the dynamic response and failure modes of slopes under earthquake motions (Chen, 2016; Fan, 2016).

To clarify the dynamic evolution and failure mechanism of rock slopes with complex geological structures, shaking table tests are designed and carried out in this study based on the engineering background of the slope response of the Jinsha River Bridge. The tests imitate the slope, including its penetrating weak structural surface and steep structural surface on the trailing edge. The dynamic

response characteristics of a rock slope with a bedding weak structural surface and steep structural surface on the trailing edge is investigated, and a series of large-scale shaking table tests are performed. Moreover, based on an analysis of the slope safety factor, the processes that produce dynamic damage of the slope are identified. The failure mode and mechanism for the slope are also discussed.

2. Shaking Table Test

To investigate the dynamic response and dynamic evolution of a rock slope containing discontinuities under earthquake motion, model tests are conducted in this study. The slope model in the shaking table tests is scaled from the bank slope of the Jinsha River Bridge.

2.1 Case study

The Jinsha River Bridge crosses the Jinsha River. As shown in Fig. 1, it is an important bridge on the Huali highway connecting the cities of Lijiang and Huaping. The route crosses the Jinsha River at a vertical angle from east to west (as shown in Fig. 2). As the key project of the HuaLi highway, the main pile cap of the bridge is located in the middle of the slopes near the Jinsha River. The bank slope, on which the main pile cap was built, has a stepped topography due to the dip structure and flow along the river. The Huaping coast is along the bank slope, with a gradient of 20° – 30° . The exposed strata of the project area are mainly a Permian basalt formation (P2 β 3), basalt almond-shaped lithological volcano, breccia lava, and tuff. The site of the slope has a tuff structural surface and a step structural surface on the trailing edge (as shown in Fig. 3). This area can resist an earthquake with an intensity of VIII. Combined with the actual situation of the bridge, the main factors affecting the stability of the slope are the topography, stratigraphic lithology, combination of the structural surfaces, and seismic loads.

2.2 Material properties

According to the geologic conditions of the Huaping bank slope along the Jinsha River Bridge, the rock slope is assumed to be in a state of plane strain. The material characteristics of the models and test conditions should be confirmed using the law of similitude. The similarity ratio for the geometric dimensions is 375, the similarity ratio for the acceleration is 1, and the similarity ratio for the density is 1. The other physical quantities are calculated according to these similarity criteria, and are summarized in Table 1. 1

Table 1
Similarity criteria calculation

Quantity	Similarity criteria	Similarity coefficient
Geometric L	$C_L=375$	375
Acceleration a	$C_a=1$	1
Density ρ	$C_\rho=1$	1
Young's modulus E	$C_E=C_\rho C_L$	375
Poisson's ratio μ	1	1
Cohesion c	$C_c=C_\rho C_a C_L$	375
Internal friction angle φ	1	1

The results calculated with the similarity ratios indicate that a thickness of the tuff structure surface of 5 mm can be used in the test model. In order to meet this requirement, model materials are prepared by as a mixture of other materials, i.e., cement, sand, clay, and iron powder. Based on the ratio test, density test, materials test, and three static tri-axial tests, the selected mass ratio of cement, sand, clay, iron powder, mixture (admixture and water reducing agent) and water is 0.325:17:9:0.4:0.03:5. The physical parameters of this mixture are listed in Table 2. The tuff material on the structural surface is modeled with a PVC expansion sheet to obtain a similar cohesion of 21.1 kPa and internal friction angle of 23.2°.

Table 2
Physical-mechanical parameters of material parameters of the slope

	Rock material	Density $\gamma/kN \cdot m^{-3}$	Young's modulus E/MPa	Cohesion c/kPa	Internal friction angle $\varphi/^\circ$
Physical parameters (rock material)	Basalt	30	69000–82500	11250–14440	46.3–46.9
	Tuff	\	\	\	29
Results of similarity criteria calculation	Basalt	30	184–220	30-38.5	46.3–46.9
	Tuff	\	\	\	29
Physical parameters (similarity material)	Basalt	20.4	100	48.43	40.69
	Tuff	\	\	\	23.2

2.3 Scale model

The model is 1.3 m in height and weighs more than 7 tons (as shown in Fig. 4). There are many challenges in construction of a model of this size. If the model is poured as a whole, the curing time will be excessively long. Because different areas in the model have different curing times, it is difficult to control the strength of the simulation material. In addition, it is difficult to place the sensor in the center of the model. Therefore, a special construction method is used to address these problems. The model is split into 224 blocks, and each block is poured with a corresponding mold. The curing times of all blocks are then precisely controlled. Typical blocks are shown in Fig. 5. To simulate the tuff structural surface, a PVC expansion sheet was inserted in the block during the corresponding stage. A typical block containing the tuff structural surface is shown in Fig. 5b. To simulate the step structural surface in the trailing edge, sand was inserted in the block during the corresponding stage. A typical block containing a step structural surface in the trailing edge is shown in Fig. 5c. After completion of the model, the PVC expansion sheet is connected to form the same shape as the tuff structural surface. Some cracks are used to simulate the step structural surface on the trailing edge, as shown in Fig. 5c. These cracks are cut with a 5-mm-thick iron sheet and filled with sand. After the block is poured, it is cured for 5d in a dry, cool environment.

To clarify the dynamic response of the rock slope, a simplified model was established and simulated. The model slope had a size of 280×140 cm and a height of 130 cm (shown in Fig. 3). The slope model was constructed with prefabricated blocks, which were assembled in seven layers. The angles of the structural plane and trailing edge of the steep structural surface slope in the model material were 30° and 75°, respectively. The slope model is shown in Fig. 6.

2.4 Measurements

The acceleration measurement setup is shown in Fig. 7. First, 20 accelerometers were arranged in the slope; accelerometers A8, A12, A15, A18, A22, A23, A24, and A25 were placed on the slope surface, while the other accelerometers were embedded at various depths in the slope. The accelerometers used are able to collect acceleration data in three directions simultaneously (as shown in Fig. 8). The frequency range of the acceleration sensors is 0–1500 Hz in the horizontal direction and 0–800 Hz in the vertical direction; the sensitivity is approximately $66 \text{ mV/m}\cdot\text{s}^{-2}$ with a range of $\pm 20 \text{ m/s}^2$. An additional buffer layer with a thickness of 10cm was designed to minimize the effects of the bottom boundary.

2.5 Input motions

The waveform was synthesized by a local earthquake prediction department based on local historical earthquake data and geological characteristics. The time history and response spectrum are shown in Fig. 9. The dominant frequency of the artificial synthetic wave was 4.5–5.5 Hz. The seismic waves were loaded horizontally in the tests. The working conditions of the tests are summarized in Table 3.

Table 3
Cases of test

No	Exciting direction	Earthquake intensity degree	$a_{\max}(\text{m}\cdot\text{s}^{-2})$
1	horizontal(x)	6	0.37
2	horizontal(x)	7	0.74
3	horizontal(x)	8	2.97
4	horizontal(x)	9	4.46

3. Dynamic Evolution Under Earthquake Loads

The acceleration response of the slope is the core parameter for evaluating the slope seismic dynamic response (Fan et al., 2016a; Dong et al., 2011). The peak ground acceleration (PGA) is the maximum acceleration value of each measuring point, and the acceleration amplification coefficient (M_{PGA}) is the ratio between the PGA and the peak acceleration of the vibration table mesa. To determine the dynamic response and dynamic evolution of the rock slope under earthquake loads, the PGA, M_{PGA} , and safety factors were calculated and analyzed.

3.1. Characteristics of the dynamic response

Figure 10 shows that the acceleration amplification effect mainly occurs on the slope surface, and the maximum acceleration occurs at the top of slope. It can be concluded that the seismic wave propagation is affected by the structural surface in the bedrock body with discontinuous structural planes such as weak inter layers, cracks, and faults. The seismic wave field is superimposed on the structural surface and the slope surface. As it is affected by the stepped slope, the acceleration amplification factor alternates with the slope size.

The M_{PGA} value reached 3.7 at the top of the slope when the seismic wave was loaded in the horizontal direction. By comparing the PGA distribution with different earthquake motions, it can be observed that the amplification effect area is upwards from the slope surface to the top of the slope. Therefore, an amplified area of dynamic response occurs at the top of the slope, which means that the materials were unstable. Cracks and failure will first appear at the top of the slope under seismic loading. The M_{PGA} is smaller under the structural surface than above the surface. Thus, the existence of the structural surface can be considered to cause a mutation in the position of the acceleration response, which is not conducive to the slope stability.

The M_{PGA} distribution only reflects the distribution of the acceleration response of the slope for each case. In order to make a quantitative comparison between the dynamic responses of different cases, the history line for the M_{PGA} of the accelerometers in different cases is plotted, as shown in Fig. 11. The M_{PGA} gradually increases along the height and the surface of the slope. With a gradual increase in the input

seismic wave, the acceleration response of the slope decreases. When the intensity of the input wave reaches an intensity of VIII, the acceleration amplification coefficient of the slope no longer changes. Thus, the slope rock mass can be considered to have entered the plastic deformation stage under an earthquake of intensity VIII.

3.2 Characteristics of dynamic evolution

Figure 12 shows the relationship between M_{PGA} and earthquake intensity (amplitude of the input wave) in the horizontal direction. To clarify the dynamic evolution and failure process of the rock slope, the slope body above the tuff structural surface was selected as the research object. The M_{PGA} of the slope body were then analyzed. Figure 12 shows the evolution process of the failure and an inflexion point can be observed when input motion is 2.97 m/s^2 , which can be considered to comprise three stages: Stage 1 is the elastic stage ($< 2.97 \text{ m/s}^2$), Stage 2 is the plastic stage ($2.97\text{--}4.46 \text{ m/s}^2$), and Stage 3 is the damage stage ($> 4.46 \text{ m/s}^2$). It can be observed that the rate of decrease of M_{PGA} gradually slows with increasing earthquake intensity. In Stage 1, the M_{PGA} decreases rapidly because no deformation or damage occurs in the slope. When the M_{PGA} has decreased to a certain degree, numerous cracks appear in the slope surface. These cracks then extend, deepen, and tend to connect. Finally, in Stage 3, the M_{PGA} exhibits a sudden increase, which indicates the beginning of the occurrence of failure damage.

3.3. Stability analysis

In the shaking table tests, the sliding surface and landslide body of the model are clear. The safety factor can be calculated by considering the inertial force. In this method, the safety factor for the occurrence of sliding on the landslide body is used to analyze the stability of the rock slope. The slide failure movement patterns mainly include sliding along the surface and sliding along the two sides. In the tests, the landslide body is subjected to gravity, inertial force, and friction. The safety factor of the landslide body can be estimated when the geometry, failure mode, and sliding surface of the rock slope have been identified. The sliding body is divided into several blocks for calculation of the safety factor based on the amplification effect difference of slope body above structural surface, as shown in Fig. 11. The difference in the amplification effect represents the inequivalent force of slope body at different positions. The inertial force of each block can be obtained from one of the acceleration sensors in the block. Based on the M_{PGA} distribution, the landslide body is divided into three parts, as shown in Fig. 13. The forces between blocks can be neglected. The anti-slip force can be obtained from the normal force and the friction angle of the PVC expansion sheet. Calculating the inertial force at each moment, the maximum value obtained represents the most dangerous moment for each case. The safety factor is calculated using the equation below:

$$K_s = \frac{\sum_{i=1}^n F_{Ni} \tan \varphi_i}{[\sum_{i=1}^n (PGA \tan \varphi_i + F_{Wi} \sin \varphi_i)]_{max}}$$

where F_{Ni} is the normal force between two sides of the structure surface, ϕ_i is the internal friction angle of the PVC material, PGA is obtained from one of the acceleration sensors in the block, and F_{Wi} is the gravity of each block.

Calculation of the safety factor is based on three different values obtained from the accelerometers. The safety factor (K_s) is calculated from the most dangerous moment. The evolution of the safety factor is shown in Fig. 14. It can be seen that K_s decreases sharply when input motion changes from 0.37 m/s^2 to 0.74 m/s^2 , while it decreases gradually from 0.74 m/s^2 to 2.97 m/s^2 , with $K_s > 1.0$. Additionally, the safety factor calculated for the three segments are quite similar, which means that segmentation method does not significantly affect the calculation results. Moreover, K_s for the three blocks are all less than 1.0 when the acceleration reaches 4.46 m/s^2 , which means the surface slope is unstable. Compared to the failure mechanism of the model, the safety factor is a good reflection of the failure mode of the slope. Based on these results, the evolution process of the landslide can be divided into three stages. The first stage is an elastic stage ($K_s = 1.6\text{--}4.7$). In this stage, the rock materials of the slope are in an elastic state. The second stage is a plastic stage ($K_s = 0.8\text{--}1.6$), which indicates a dangerous moment for the slope. Low magnitude earthquakes or rainfall can easily cause landslides in this stage. The last stage is the damage stage ($K_s < 0.8$), in which landslides occur.

4. Failure Mechanism

4.1. Failure process analysis

Based on the similar failure processes observed in various models, the failure process of a rock slope can be characterized by three notable features (Huang et al., 2013). First, a crack near the top surface is observed. Second, with increasing input acceleration, the cracks extend and tend to connect. Finally, the top area of the slope will collapse and landslides will occur. To describe the failure mode of the model, any cracks or deformation present are recorded by photographs at the end of each test. The development of cracks at accelerations of less than 4.46 m/s^2 is shown in Fig. 15. Before the input acceleration reaches 0.74 m/s^2 , a few cracks can be identified near the slope surface. The failure modes of the slope model are mainly caused by the occurrence and deepening of these cracks. When the input acceleration is between 2.97 m/s^2 and 4.46 m/s^2 , the cracks continue to deepen and extend gradually, and a few penetrating cracks occur with local spalling occurring near the slope surface. A large number of cracks can be identified near the tuff structural surface, indicating a significant shear failure mode.

4.2. Failure mode analysis

Failure occurred in the model when the horizontal input acceleration reached 4.46 m/s^2 , and a photo of the model after failure is shown in Fig. 16. The cracks and deformation in the model observed during the process of removal are the main basis for judging the sliding surface, as shown in Fig. 17. Figure 17 shows that the shear outlet position is located on the slope surface 60 cm above the bottom of the slope.

There are dense transverse and longitudinal cracks along the slip surface, and distinct downward dislocations have formed at the top of the slope. The location of the slip surface and the tuff structural surface are very similar. It can be concluded that the tuff structural surface plays a controlling role in the position of landslides and cutting.

5. Conclusions

a) A series of shaking table tests were designed and performed to study the stability of a rock slope with discontinuities. Special construction technology was employed to achieve an accurate simulation. The shaking table tests successfully showed the failure process for landslides under earthquake motions. The deformation and damage mainly developed within a zone of shallow depth in the upper part of the slope. The height and slope structure have a significant impact on the M_{PGA} of the slope. The M_{PGA} increases with increasing height, and reaches a maximum at the top of the slope. The M_{PGA} of the slope surface is greater than that inside the slope. Thus, it can be considered that the existence of the structural surface causes a mutation in the position of the acceleration response, which is not conducive to slope stability.

b) Under the impact of earthquakes, the evolution process of damage deformation of the slope can be divided into three stages: Stage 1 (elastic stage), Stage 2 (plastic stage), and Stage 3 (damage stage). These stages are related to the appearance of numerous cracks in the slope surface. These cracks then extend, deepen, and tend to connect. The sliding mode thus occurs as below: before the earthquake intensity reaches 0.74 m/s^2 , a few cracks can be identified near the slope surface; when the earthquake intensity is between 2.97 m/s^2 and 4.46 m/s^2 , the cracks continue to deepen and extend gradually, and a few penetrating cracks occur with local spalling occurring near the slope surface; failure occurs when the horizontal earthquake intensity reaches 4.46 m/s^2 .

c) Slope safety factors were calculated based on pseudo static analysis and used to describe the failure process. A good correspondence could be observed between the safety factors and the failure mode of the slope. K_s decreases sharply from 0.37 m/s^2 to 0.74 m/s^2 , while it decreases gradually from 0.74 m/s^2 to 2.97 m/s^2 , with $K_s > 1.0$. Moreover, the K_s values for the three blocks are all less than 1.0 when the earthquake intensity is 4.46 m/s^2 . The damage evolution process of the slope can be identified, and includes three stages: an elastic stage ($K_s = 1.6-4.7$), a plastic stage ($K_s = 0.8-1.6$), and a damage stage ($K_s < 0.8$). The plastic stage is a dangerous moment for the slope. Earthquakes of low magnitude or rainfall can easily cause landslides in this stage.

6. Declarations

ACKNOWLEDGEMENTS

This work is supported by the National Key R&D Program of China (2018YFC1504504). The authors would like to express their gratitude to the Key Laboratory of Loess Earthquake Engineering, CEA Gansu Province for their helpful advice.

7. References

1. An J, Bai X, Xu J, et al. (2015) Prediction of highway blockage caused by earthquake-induced landslides for improving earthquake emergency response. *Natural Hazards*, 79(1): 511-536. DOI: <https://doi.org/10.1007/s11069-015-1859-7>
2. Babanouri N, Dehghani H. (2017) Investigating a potential reservoir landslide and suggesting its treatment using limit-equilibrium and numerical methods. *Journal of Mountain Science*, 14(3): 432-441. DOI: <https://doi.org/10.1007/s11629-016-3898-2>
3. Che A, Yang H, Wang B, et al. (2016) Wave propagations through jointed rock masses and their effects on the stability of slopes. *Engineering Geology*, 201: 45-56. DOI: <https://doi.org/10.1016/j.enggeo.2015.12.018>
4. Chen Z, Hu X, Xu Q. (2016) Experimental study of motion characteristics of rock slopes with weak intercalation under seismic excitation. *Journal of Mountain Science*, 13(3): 546. DOI: <https://doi.org/10.1007/s11629-014-3212-0>
5. Dai F, Xu C, Yao X, et al. (2011) Spatial distribution of landslides triggered by the 2008 Ms 8.0 Wenchuan earthquake. *Journal of Asian Earth Sciences*, 40(4): 883-895. DOI: <http://dx.doi.org/10.1016/j.jseaes.2010.04.010>
6. Huang R, Li W. (2009) Analysis of the geo-hazards triggered by the 12 May 2008 Wenchuan Earthquake, China. *Bulletin of Engineering Geology and the Environment*, 68(3): 363-371. DOI: <https://doi.org/10.1007/s10064-009-0207-0>
7. Fan G, Zhang J, Fu X, et al. (2016a) Dynamic failure mode and energy-based identification method for a counter-bedding rock slope with weak intercalated layers. *Journal of Mountain Science*, 13(12): 2111-2123. DOI: <https://doi.org/10.1007/s11629-015-3662-z>
8. Fan G, Zhang J, Wu J et al. (2016b) Dynamic response and dynamic failure mode of a weak intercalated rock slope using a shaking table. *Rock Mechanics and Rock Engineering*, 49(8): 3243-3256. DOI: <https://doi.org/10.1007/s00603-016-0971-7>
9. Lee D, Yang Y, Lin H. (2007) Assessing slope protection methods for weak rock slopes in Southwestern Taiwan. *Engineering Geology*, 91(2): 100-116. DOI: <https://doi.org/10.1016/j.enggeo.2006.12.005>
10. Li X, He S. (2009) Seismically induced slope instabilities and the corresponding treatments: the case of a road in the Wenchuan earthquake hit region. *Journal of Mountain Science*, 6(1): 96-100. DOI: <https://doi.org/10.1007/s11629-009-0197-1>
11. Li X, Zuo Y, Zhuang X, et al. (2014) Estimation of fracture trace length distributions using probability weighted moments and L-moments. *Engineering Geology*, 168: 69-85. DOI: <https://doi.org/10.1016/j.enggeo.2013.10.025>
12. Lin M, Wang K. (2006) Seismic slope behavior in a large-scale shaking table model test. *Engineering Geology*, 86(2): 118-133. DOI: <https://doi.org/10.1016/j.enggeo.2006.02.011>

13. Liu H, Xu Q, Li Y. (2014) Effect of lithology and structure on seismic response of steep slope in a shaking table test. *Journal of Mountain Science*, 11(2): 371. DOI: <https://doi.org/10.1007/s11629-013-2790-6>
14. Pépin N, Aubertin M, James M. (2012) Seismic table investigation of the effect of inclusions on the cyclic behavior of tailings. *Canadian Geotechnical Journal*, 49(4): 416-426. DOI: <https://doi.org/10.1139/t2012-009>
15. Quecedo M, Pastor M, et al. (2004) Numerical modelling of the propagation of fast landslides using the finite element method. *International Journal for Numerical Methods in Engineering*, 59(6):755–794. DOI: <https://doi.org/10.1002/nme.841>
16. Sahoo S, Manna B, Sharma K. (2015) Stability analysis of steep nailed slopes under seismic condition using 3-D finite element method. *International Journal of Geotechnical Engineering*, 9(5): 536-540. DOI: <https://doi.org/10.1179/1939787914y.0000000084>
17. Shen J, Karakus M. (2013) Three-dimensional numerical analysis for rock slope stability using shear strength reduction method. *Canadian geotechnical journal*, 51(2): 164-172. DOI: <https://doi.org/10.1139/cgj-2013-0191>
18. Tang C. (2010) Activity Tendency Prediction of Rainfall Induced Landslides and Debris Flows in the Wenchuan Earthquake Areas. *Journal of Mountain Science*, 28(3): 341-349.
19. Wakai A, Tanaka N, Abe S, et al. (2008) Large-area damage prediction system based on finite element method for risk assessment of seismic slope failure in mountains area. *Journal of the Japan Landslide Society*, 45(3): 207-218. DOI: <https://doi.org/10.3313/jls.45.207>
20. Xu B, Yan C, Xu S. (2013) Analysis of the bedding landslide due to the presence of the weak intercalated layer in the limestone. *Environmental earth sciences*, 70(6): 2817-2825. DOI: <https://doi.org/10.1007/s12665-013-2341-z>
21. Xu B, Yan C. (2014) An experimental study of the mechanical behavior of a weak intercalated layer. *Rock Mechanics and Rock Engineering*, 47(2): 791-798. DOI: <https://doi.org/10.1007/s00603-013-0420-9>
22. Yang G, Wu F, Dong J. (2012) Study of dynamic response characters and failure mechanism of rock slope under earthquake. *Chinese Journal of Rock Mechanics and Engineering*, 31(4): 696-702.
23. Yang T, Xu T, Liu H, et al. (2014) Rheological characteristics of weak rock mass and effects on the long-term stability of slopes. *Rock Mechanics and Rock Engineering*, 47(6): 2253-2263. DOI: <https://doi.org/10.1007/s00603-013-0527-z>
24. Yang X. (2009) Seismic bearing capacity of a strip footing on rock slopes. *Canadian Geotechnical Journal*, 46(8): 943-954. DOI: <https://doi.org/10.1139/t09-038>
25. Yang Z, Lan H, Gao X, et al. (2015) Urgent landslide susceptibility assessment in the 2013 Lushan earthquake-impacted area, Sichuan Province, China. *Natural Hazards*, 75(3): 2467-2487. DOI: <https://doi.org/10.1007/s11069-014-1441-8>
26. Yin Y, Wang F, Sun P. (2009) Landslide hazards triggered by the 2008 Wenchuan earthquake, Sichuan, China. *Landslides*, 6(2): 139-152. DOI: <https://doi.org/10.1007/s10346-009-0148-5>

27. Yin Y, Wang W, Zhang N, et al. (2017) The June 2017 Maoxian landslide: Geological disaster in an earthquake area after the Wenchuan Ms 8.0 earthquake. Science China Technological Sciences, 60(11): 1762-1766. DOI: <https://doi.org/10.1007/s11431-017-9148-2>

Figures

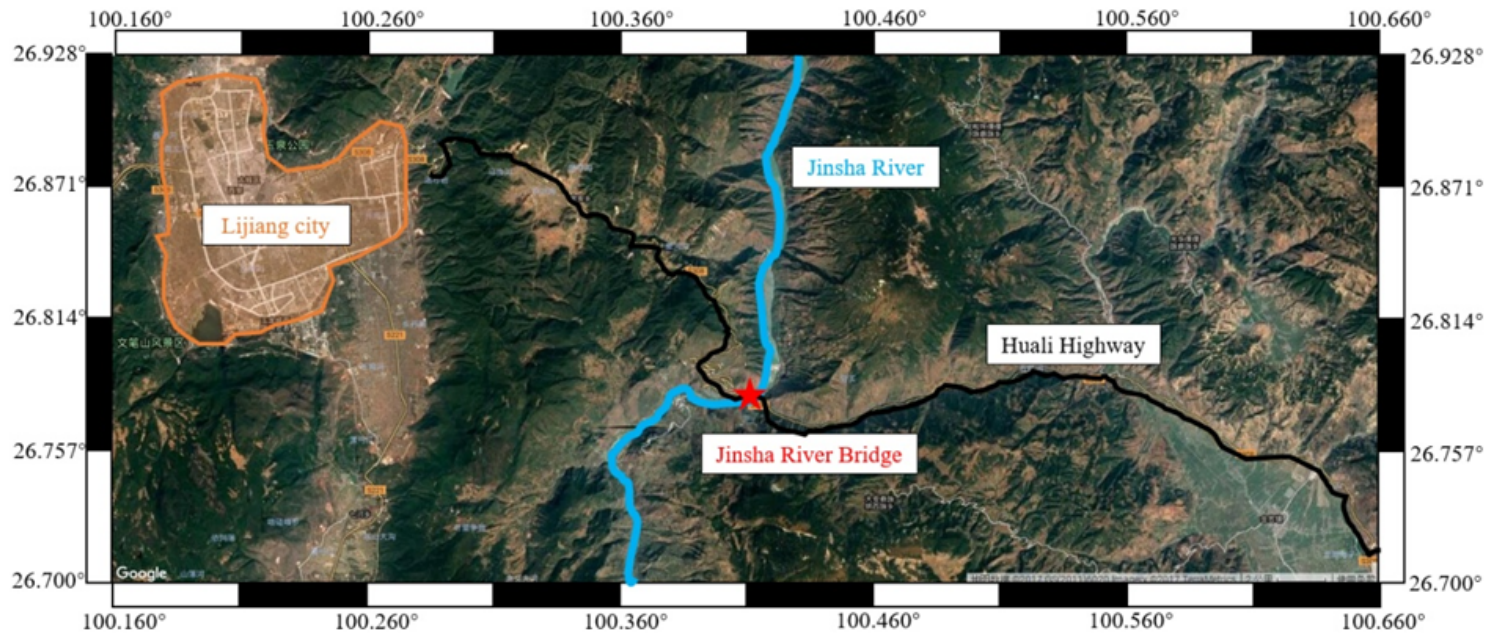


Figure 1

Location of Jinsha River Bridge

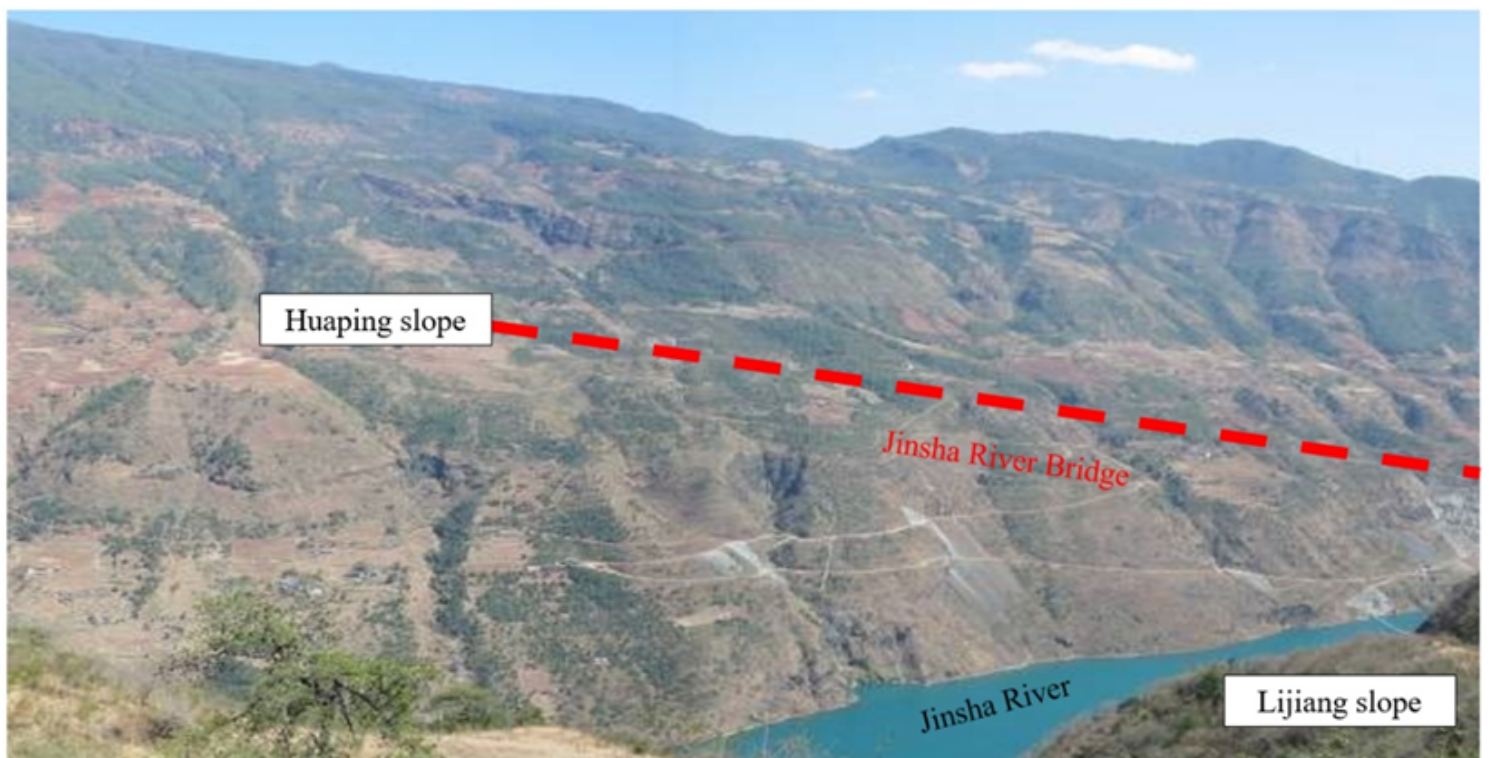
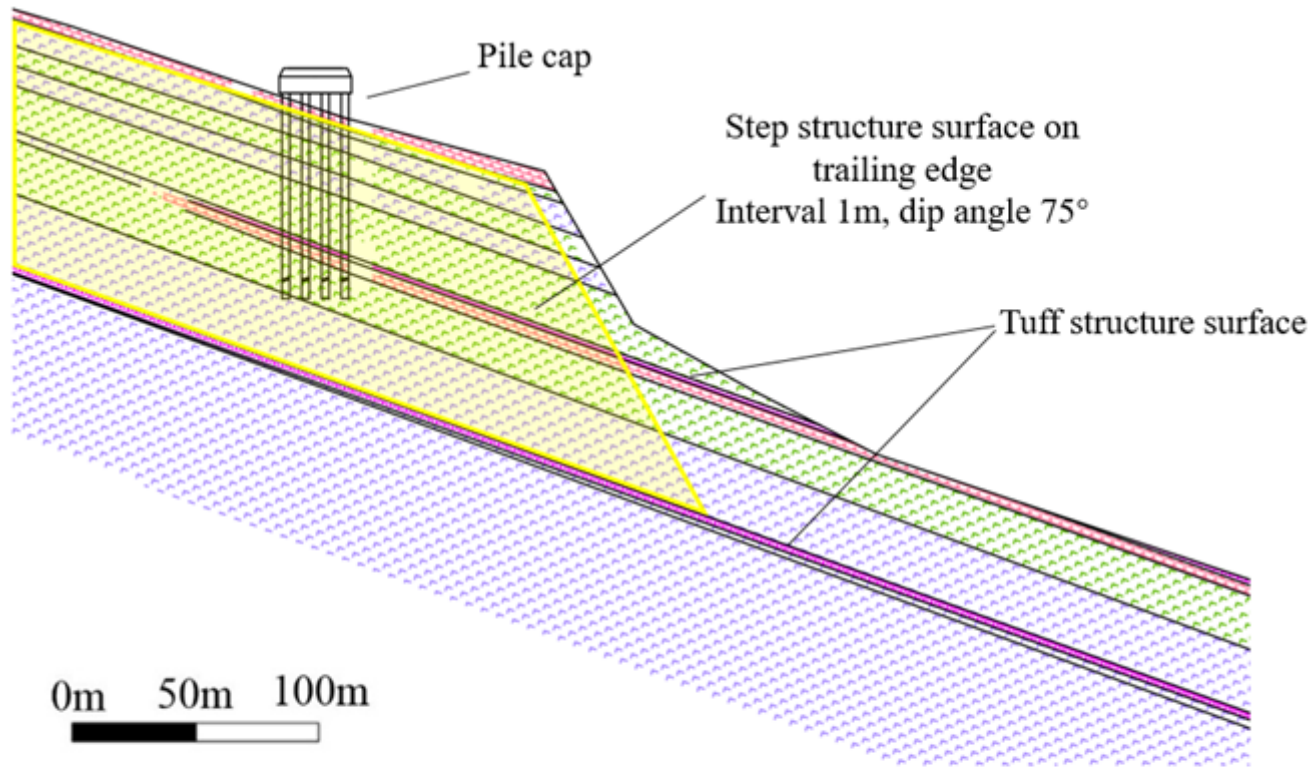


Figure 2

Topography and geomorphology of Huaping bank slope



Basalt				Breccia	Tuff
Massive	Amygdaloidal	Phenocryst	Breccia	Volcanic	Volcanic

Figure 3

Stratigraphic distribution of the slope

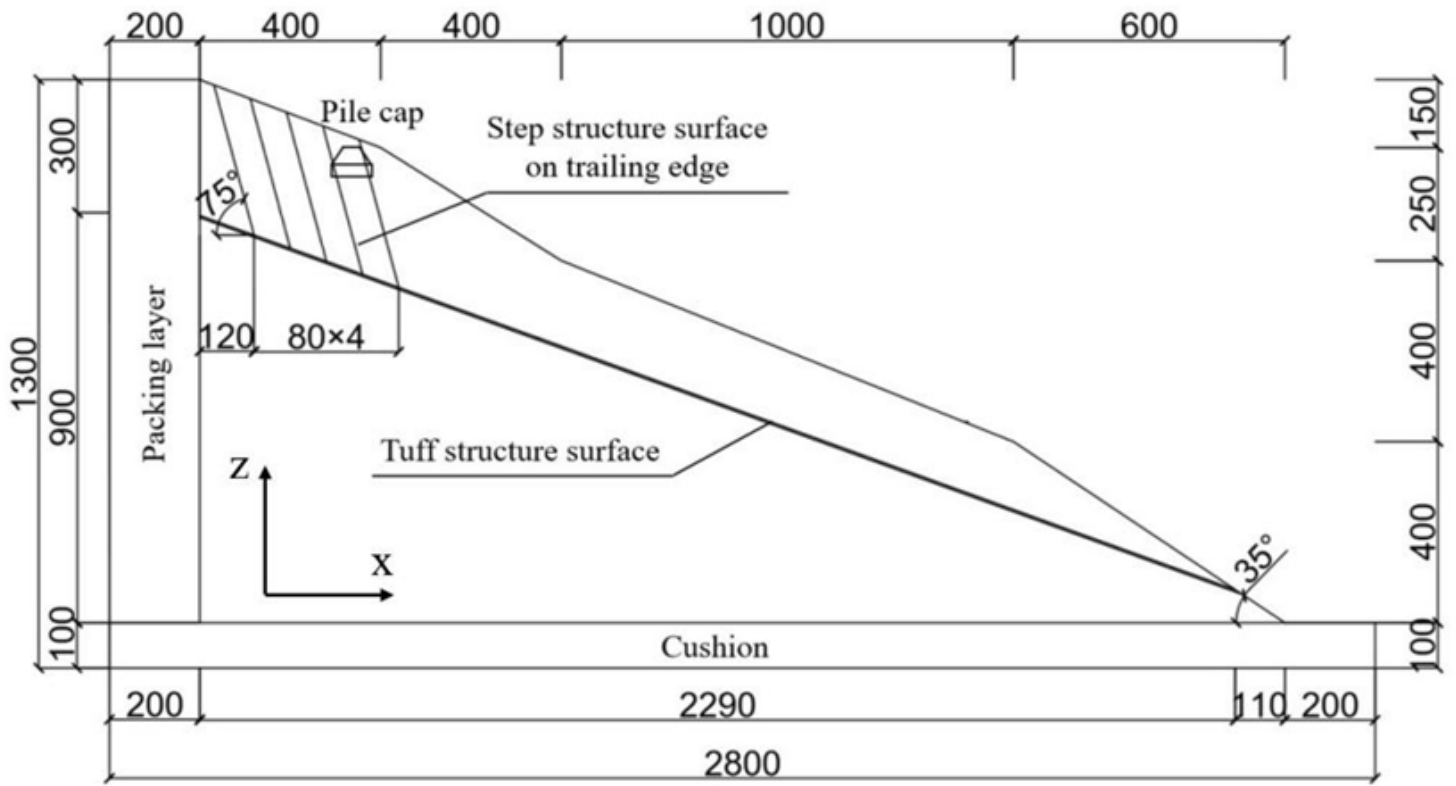


Figure 4

Scaled model (mm)



(a) Normal blocks (b) Tuff structure surface



(c) Step structure surface on trailing edge

Figure 5

Photo of the testing blocks



Figure 6

Photo of the scaled model

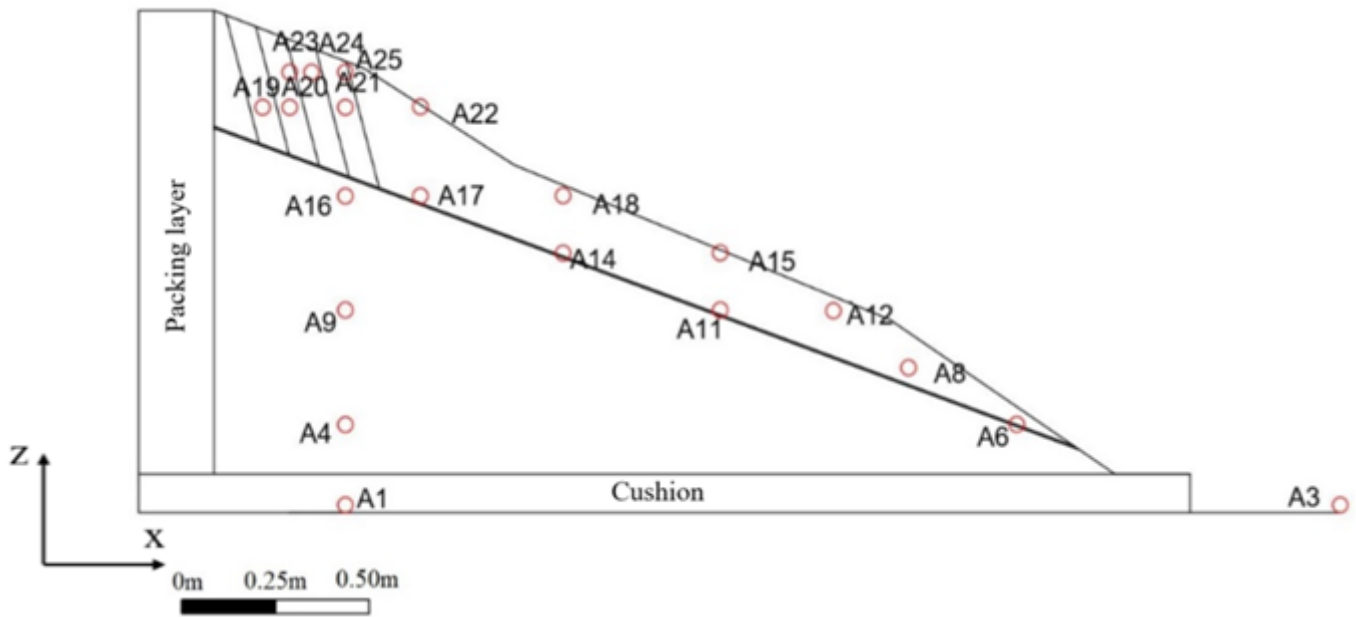


Figure 7

Measurement points

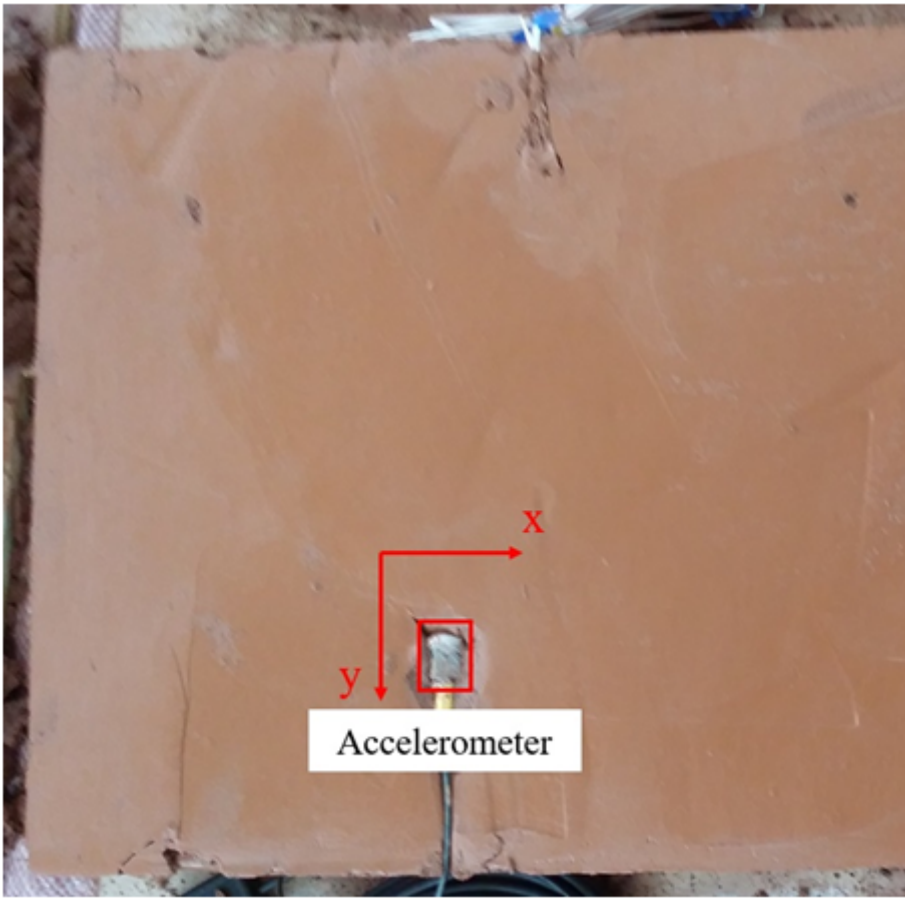
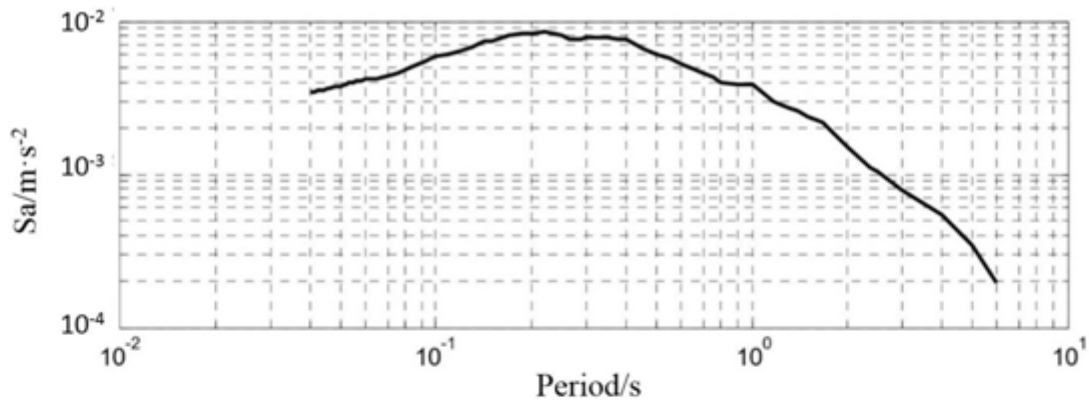
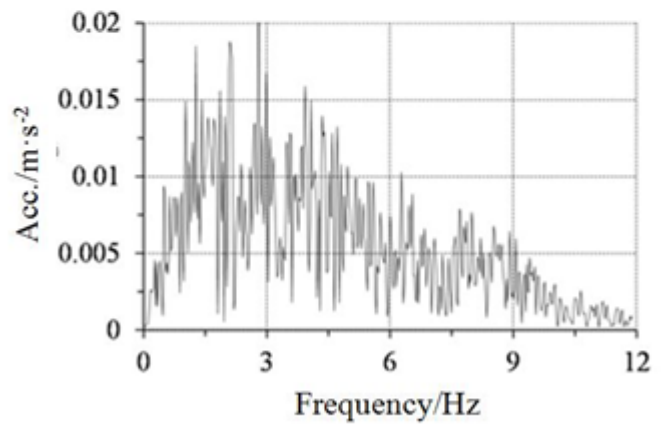
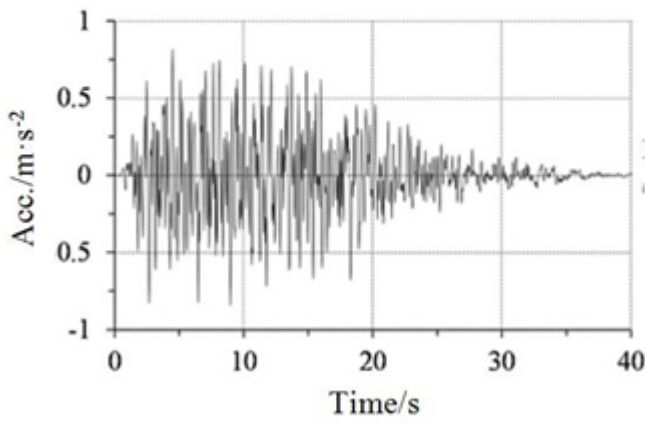


Figure 8

Install of the accelerometer



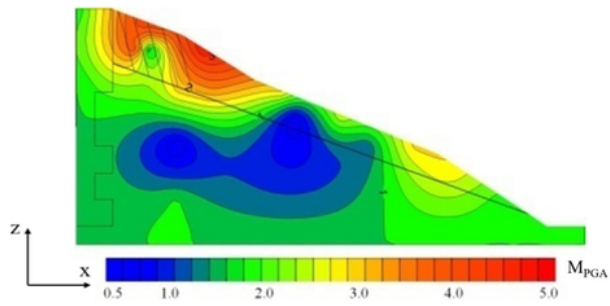
(a) The responsespectrum



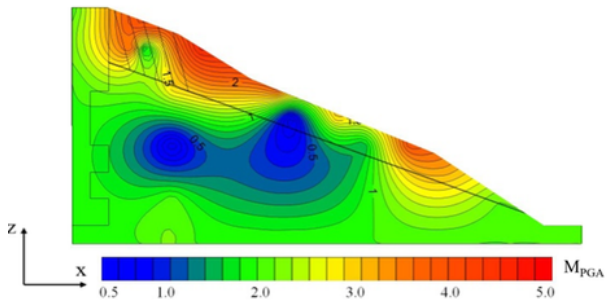
(b)Thetimehistory(c)TheFourierspectrum

Figure 9

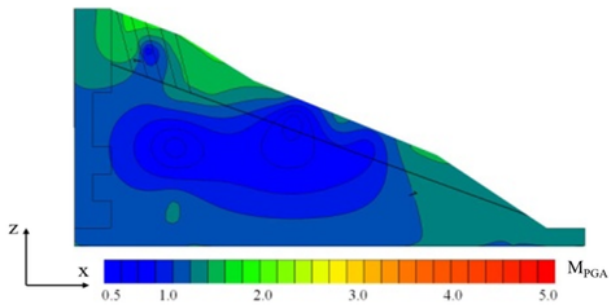
The input artificial synthetic wave



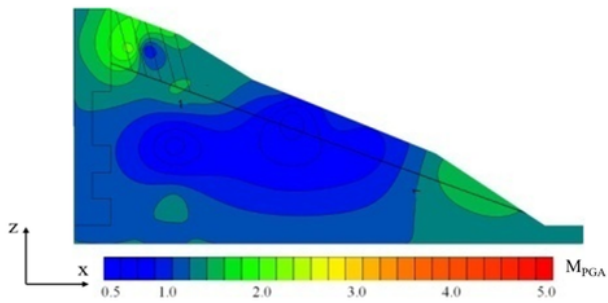
(a) 0.37m/s^2



(b) 0.74m/s^2



(c) 2.97m/s^2



(d) 4.46m/s^2

Figure 10

MPGA distribution under artificial input motion

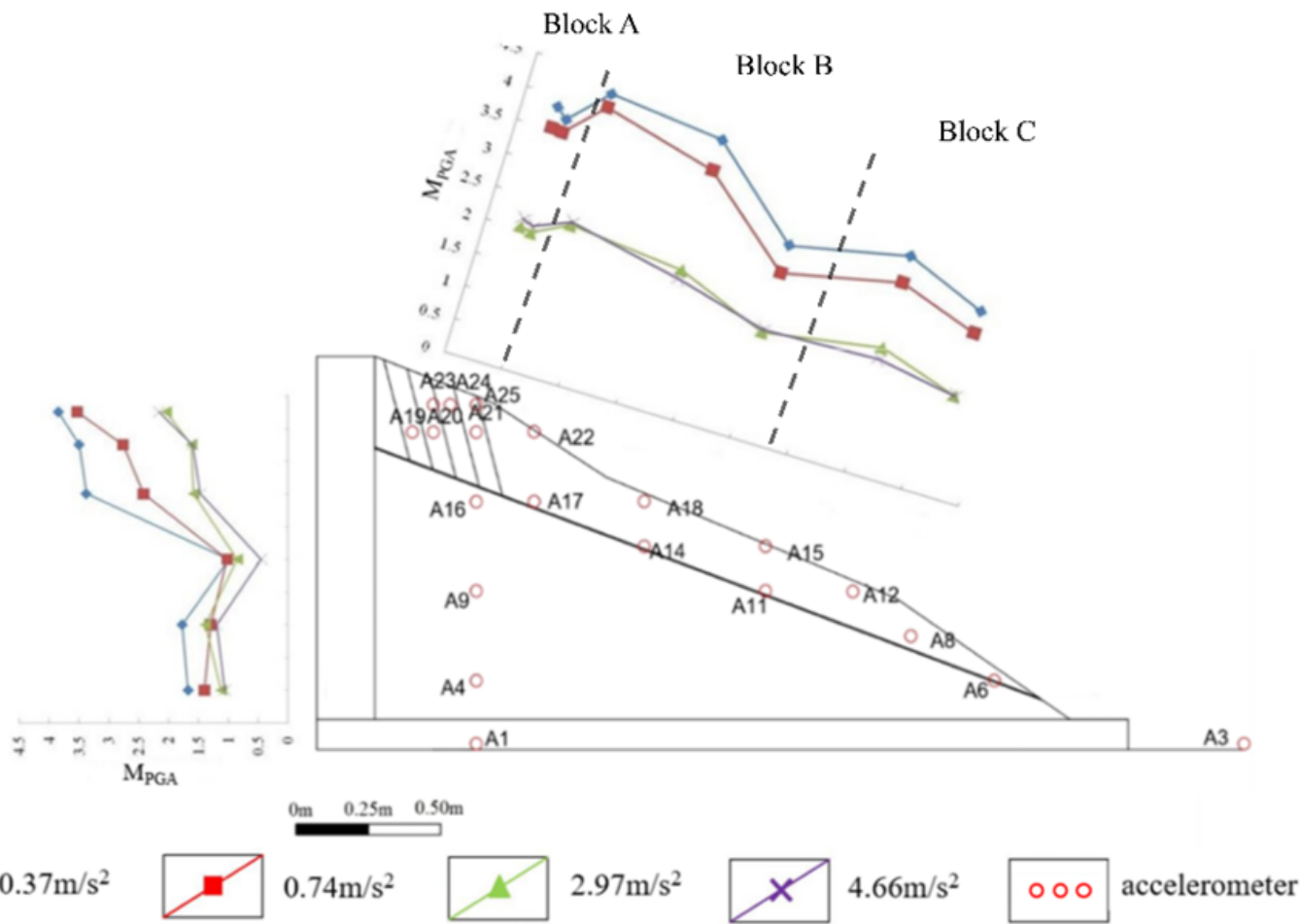


Figure 11

Acceleration response along slope

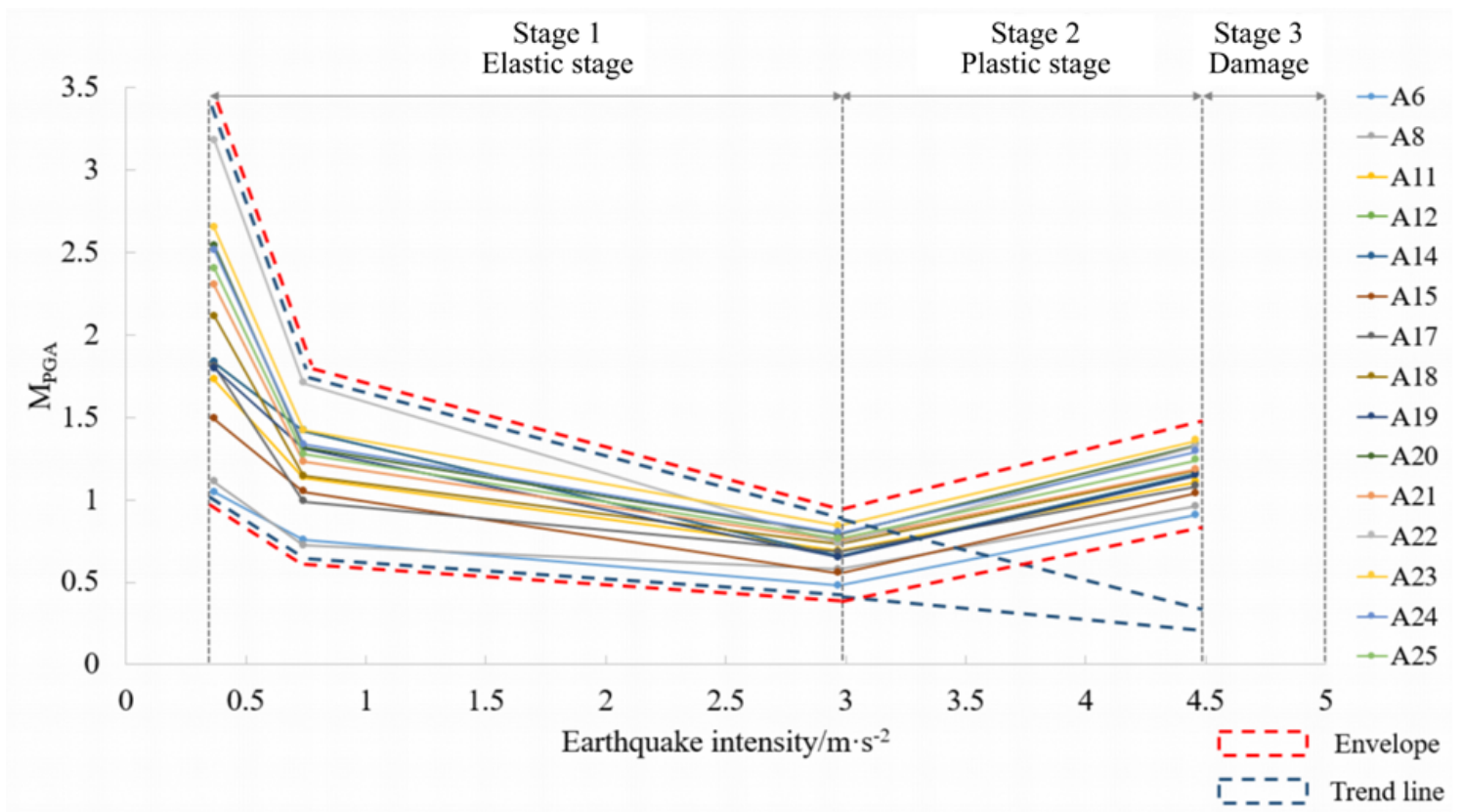


Figure 12

Relationship between MPGA and earthquake intensity

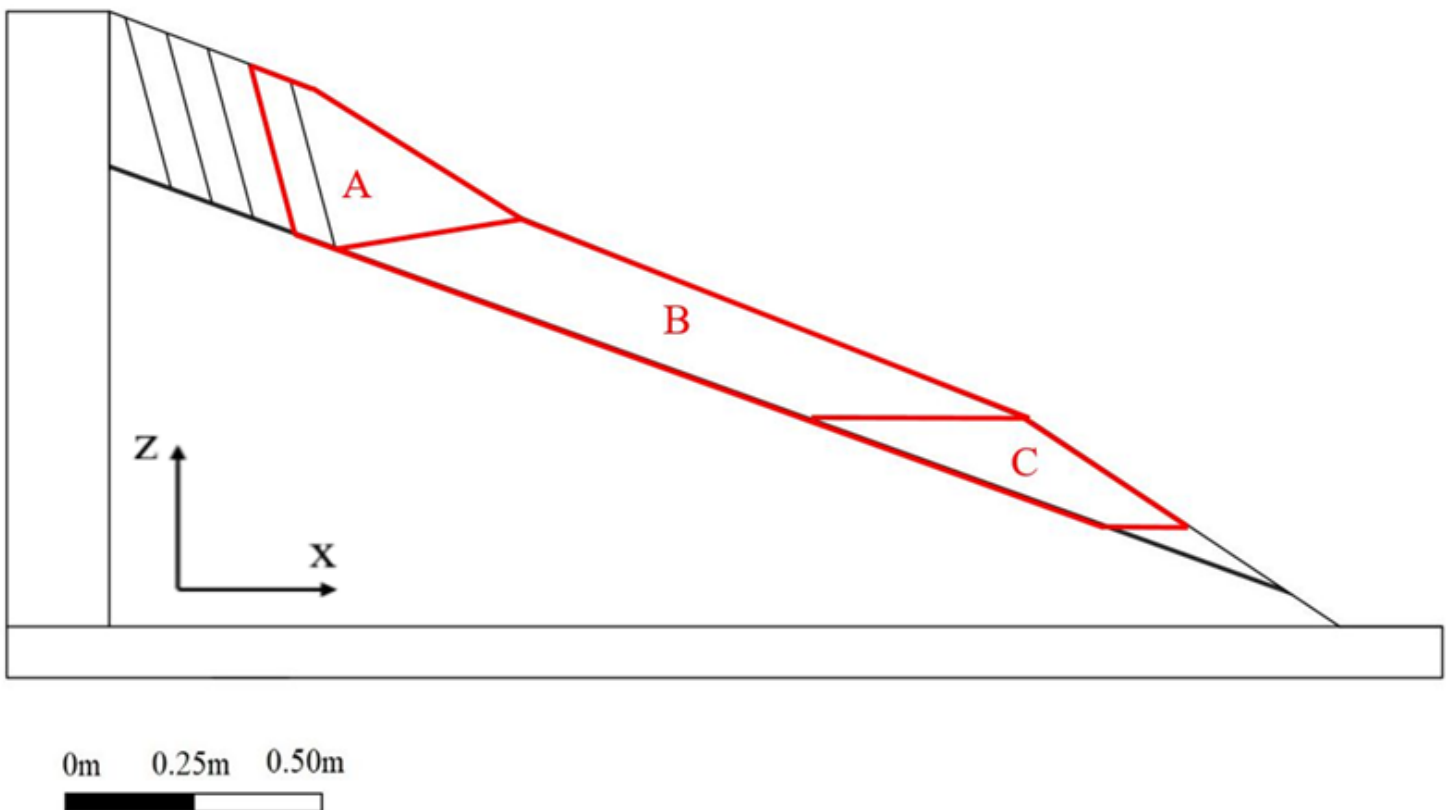


Figure 13

Divide for calculating the safety factor

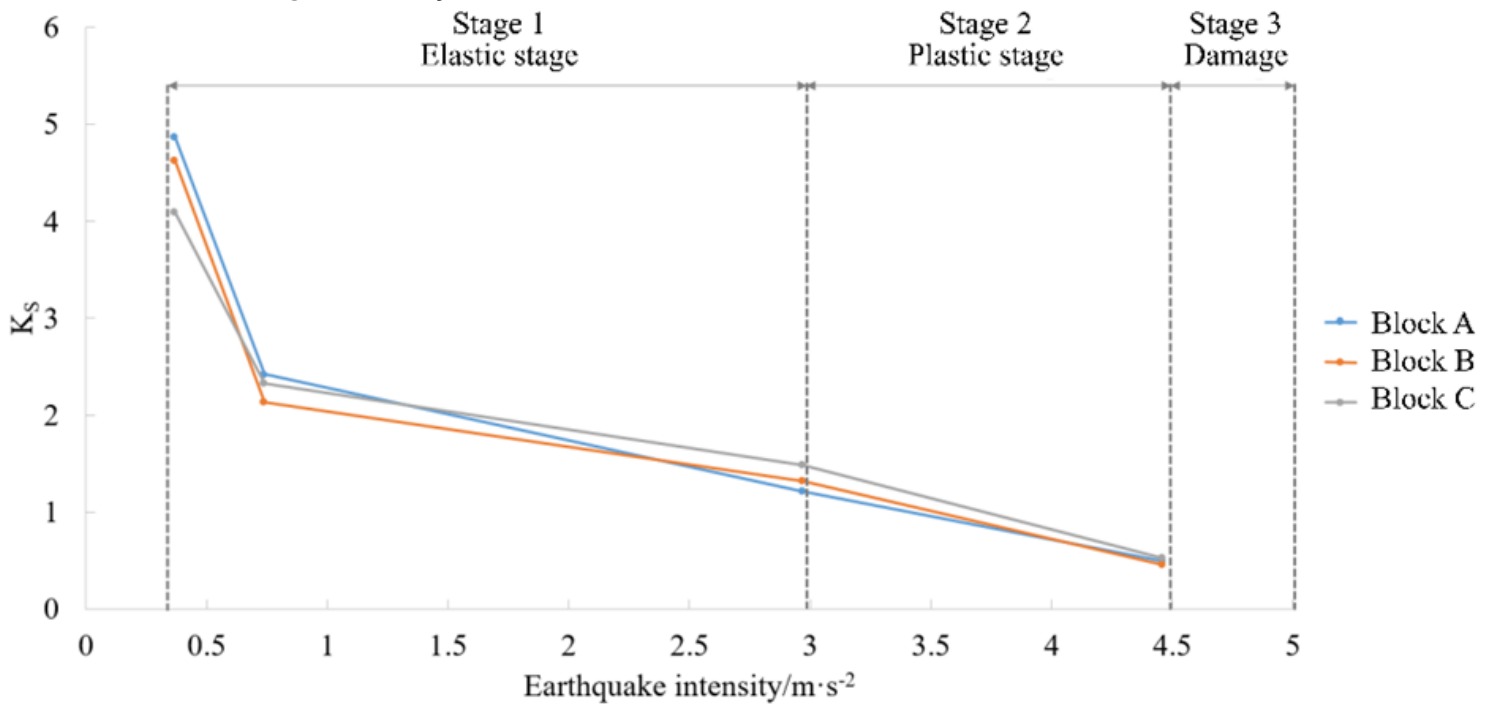


Figure 14

Relationship between K_s and earthquake intensity

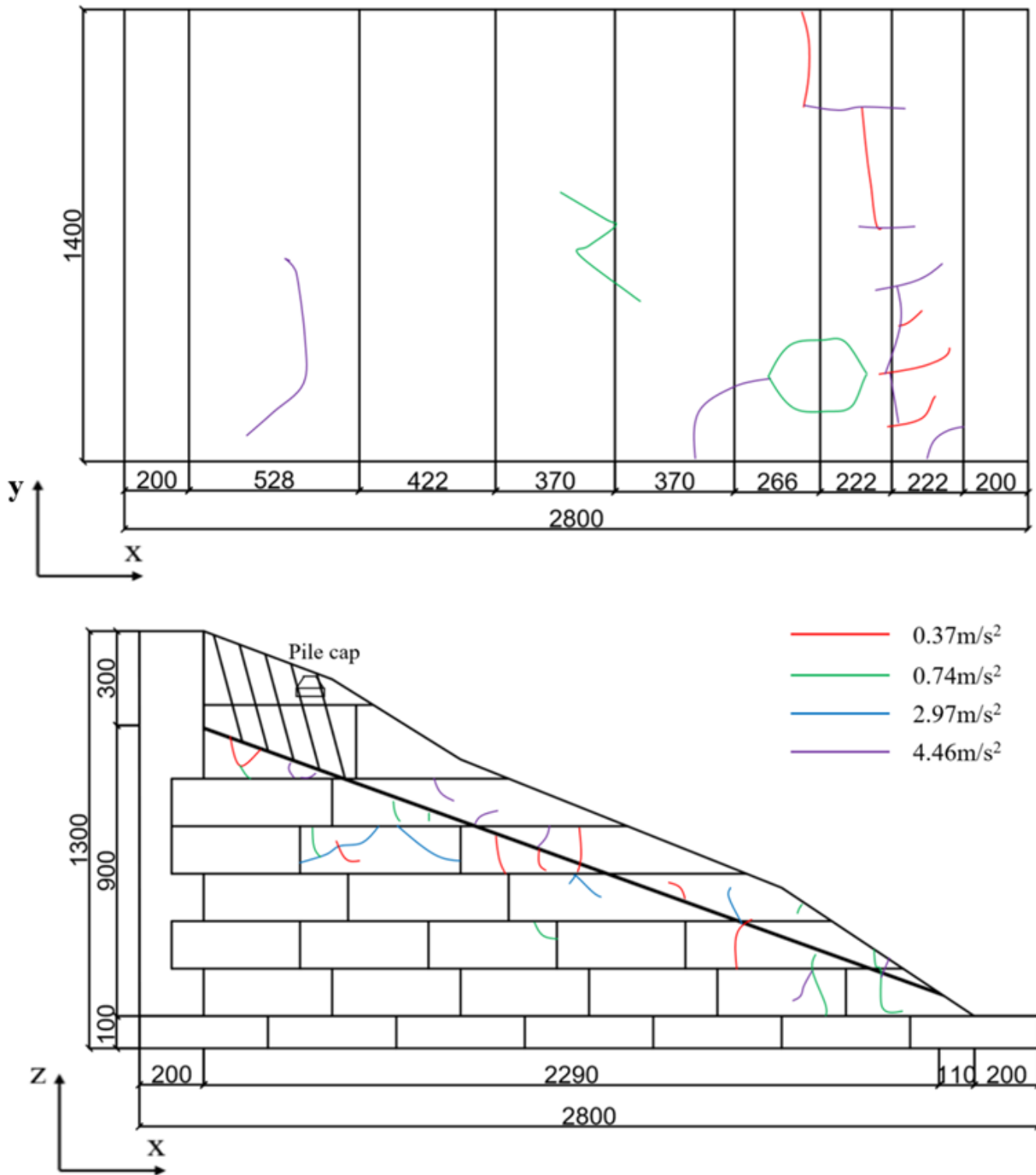


Figure 15

Description of failure process

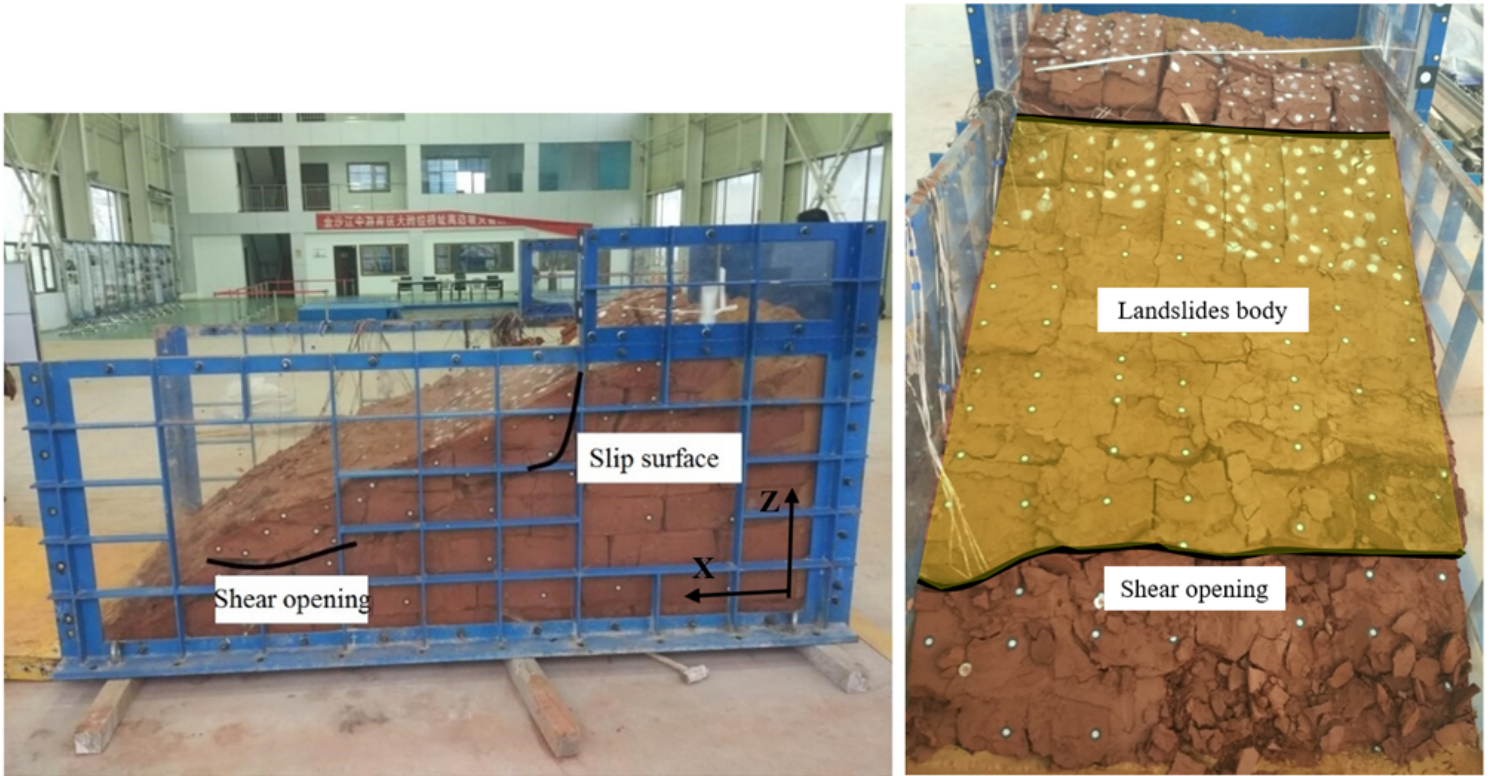


Figure 16

Photograph of model after shaking

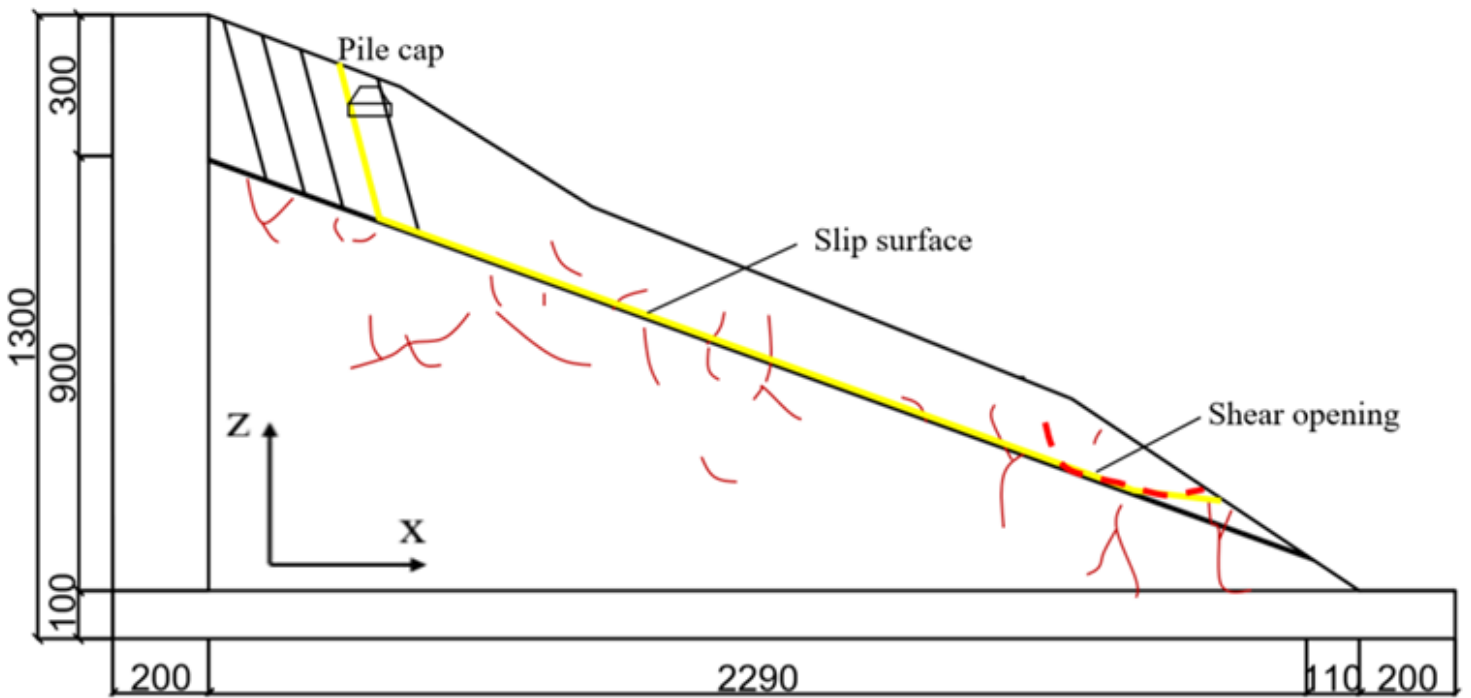


Figure 17

Deformation characteristics of the slope